CHALMERS
UNIVERSITY OF TECHNOLOGY

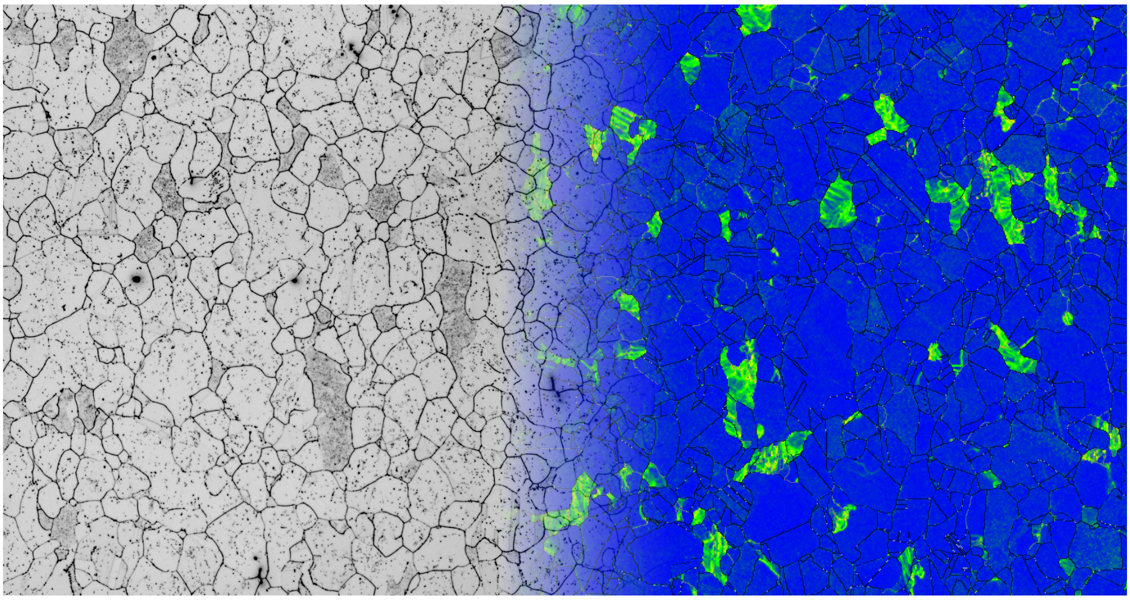

Influence of Processing Parameters, Feedstock and Heat Treatment on the Microstructure of PBF-LB 316L Stainless Steel

Master's thesis in Material Chemistry

Petter Jacobsson

Department of Industrial and Materials Science
CHALMERS UNIVERSITY OF TECHNOLOGY
Gothenburg, Sweden 2026
www.chalmers.se

Master's thesis 2026

Influence of Processing Parameters, Feedstock and Heat Treatment on the Microstructure of PBF-LB 316L Stainless Steel

Petter Jacobsson

CHALMERS
UNIVERSITY OF TECHNOLOGY

Department of Industrial and Materials Science
Chalmers University of Technology
Gothenburg, Sweden 2026

Influence of Processing Parameters, Feedstock and Heat Treatment on the Microstructure of PBF-LB 316L Stainless Steel
Petter Jacobsson

Supervisor:	Rasmus Gunnerek, Industrial and Materials Science, Chalmers
	Tommy Sand, Vattenfall
	Fredrik Gustavsson, Vattenfall
Examiner:	Uta Klement, Industrial and Materials Science, Chalmers

Degree project report 2026
Department of Industrial and Materials Science
Chalmers University of Technology
SE-412 96 Gothenburg
Sweden
Telephone +46 31 772 1000

Cover: Micrograph (left) and KAM map (right) of the same sample from print B.

Gothenburg, Sweden 2026

Influence of Processing Parameters, Feedstock and Heat Treatment on the
Microstructure of PBF-LB 316L Stainless Steel
Petter Jacobsson
Department of Industrial and Materials Science
Chalmers University of Technology

Abstract

The increasing demand for reliable and rapidly deployable spare parts in highly regulated industries such as nuclear power has accelerated the interest in additive manufacturing (AM) of stainless steels. In this work, the influence of heat treatment, process parameters, powder type and part geometry on the microstructure of powder bed fusion-laser beam (PBF-LB) produced 316L stainless steel was investigated. Samples using both vacuum induction gas atomized (VIGA) and gas atomized (GA) were subjected to stress relieving (SR) and solution annealing (SA) and a combination of these treatments. Microstructural evolution was characterized primarily using light optical microscopy (LOM) and quantitative image analysis, with selected samples additionally characterized by EBSD.

The results showed that stress relieving preserved the characteristic anisotropic melt pool and columnar grain structures formed during printing, while SA at 1200 °C promoted varying degrees of recrystallization depending on processing route and powder feedstock. Samples produced using GA powder exhibited extensive recrystallization and annealing twin formation after SA, whereas VIGA samples largely retained the original grain morphology despite identical HT schemes. Variations in laser power influenced melt pool geometry and porosity formation, but only limited effects on recrystallization behavior were observed. Part geometry showed minimal influence on recrystallization, although thin wall specimens were more susceptible to distortion during quenching. A custom image analysis method based on Frangi filtering was also developed to quantify grain morphology from etched LOM images.

The findings demonstrate that recrystallization behavior in PBF-LB 316L SS is strongly dependent on the combined effects of feedstock condition, thermal history and processing route. This study highlights the complexity of grain boundary engineering in the anisotropic, non-equilibrium microstructure of additively manufactured stainless steels and contributes to the understanding of post-processing strategies for the tailoring microstructure of AM components intended to replace conventional 316L parts in nuclear power plants.

Contents

List of Figures **ix**

List of Tables **xi**

1 Introduction **1**

2 Theory **3**

2.1 Additive manufacturing . . . 3
2.1.1 Powder Bed Fusion - Laser Beam (PBF-LB) . . . 3
2.1.2 Powder . . . 4
2.1.3 PBF-LB of 316L SS . . . 4
2.2 Heat treatment (HT) . . . 5
2.2.1 Grain Boundary Engineering (GBE) . . . 6
2.2.2 Strengthening mechanisms . . . 6
2.2.2.1 Grain boundary strengthening . . . 6
2.2.2.2 Solid solution strengthening . . . 7
2.2.2.3 Dislocation strengthening . . . 7
2.2.2.4 Orowan strengthening . . . 7
2.2.3 Annealing twins . . . 8
2.2.4 Second phase particles . . . 8
2.2.5 Stress relieving (SR) . . . 9
2.2.6 Solution annealing (SA) . . . 10

3 Methods **11**

3.1 Prints . . . 11
3.1.1 Print A . . . 11
3.1.2 Print B . . . 12
3.2 Characterization . . . 14
3.2.1 Image analysis . . . 14
3.2.2 Electron backscatter diffraction (EBSD) . . . 15

4 Results **17**

4.1 Influence of process parameters on microstructure after heat treatment 17
4.2 Influence of heat treatment . . . 18
4.2.1 Print A using VIGA powder . . . 18
4.2.2 Print B using GA powder . . . 19
4.3 Influence of part geometry on microstructure after heat treatment . . 22

4.4 Grain size development during heat treatment 23
4.5 Chemical analysis of powders and printed parts 24

5 Discussion **25**
5.1 Effects of multiple variables on comparability between the print campaigns 25
5.2 Degree of recrystallization 25
5.3 Powder chemistry as governing driving forces for recrystallization . . 26
5.4 Effect of stress relieve on recrystallization and twin formation 27
5.5 Grain boundary engineering 27
5.6 Image analysis based on LOM vs EBSD data 28

6 Conclusion **31**

Bibliography **33**

List of Figures

2.1 Schematic illustration of a generic PBF-LB system. After each build cycle, the build platform is lowered by one layer height. New powder is raised from the dispenser and spread across the build area by the recoater. Excess powder is captured by the overflow collector, and the laser selectively melts the newly deposited layer. The process is repeated layer by layer until the print is complete. 4
2.2 Strengthening mechanisms (a) solid solution, (b) GB strengthening with high angle grain boundary (HAGB) in green and low angle grain boundary (LAGB) in blue, (c) edge dislocation that acts as dislocation strengthening and (d) dislocation line being hindered by Orowan strengthening. 8

3.1 Build plates of the two prints, the green boundaries indicate the samples included in this study. (a) print A, printed using VIGA powder by external manufacturer and (b) print B, printed using GA powder in-house. 11
3.2 Tube furnace with argon atmosphere calibration cycle over the thermally relevant regime. The dotted line represents the reference temperature and the solid blue line the measured temperature. (1) Heating from RT to 1200 °C at 10 °C/min, (2) isothermal hold at 1200 °C, (3) isothermal hold at 900 °C, and (4) cooling from 900 °C to RT at 1.5 °C/min. 13
3.3 Schematic illustration of the sample orientation used in this work, showing the xy-plane, BDx-plane, and BDy-plane relative to the build direction (BD) in the PBF-LB process. 14
3.4 Etched sample in BD-plane analyzed with Frangi mask (a) LOM image of etched sample and (b) same image with Frangi filter overlay. . 15

4.1 Optical microscope images of etched VIGA cubes, printed with varying laser power in SR (900 °C 30 min) and SR+SA (900 °C 30 min and 1200 °C 4 h) condition. (a) 200 W SR, (b) 300 W SR, (c) 350 W SR, (d) 200 W SR+SA red arrow pointing out LoF pore and recrystallized area circled in blue, (e) 300 W SR+SA and (f) 350 W SR+SA. 17
4.2 Optical microscope images of etched samples printed using VIGA powder. xy-plane: (a) SR 900 °C 30 min and (b) SR 900 °C 30 min and SA 1200 °C 4 h. BD-plane: (c) SR 900 °C 30 min and (d) SR 900 °C 30 min and SA 1200 °C 4 h. 19

4.3 Optical microscope images of etched samples printed using GA powder. xy-plane: (a) AB, (b) SR 900 °C 30 min, (c) SR 900 °C 30 min and SA 1200 °C 4 h, (d) SA 1200 °C 4 h and (e) SA 1200 °C 24 h. BD-plane: (f) AB, (g) SR 900 °C 30 min, (h) SR 900 °C 30 min and SA 1200 °C 4 h, (i) SA 1200 °C 4 h and (j) SA 1200 °C 24 h. 20
4.4 EBSD acquired image of grain boundaries in samples from print B (a) SA 4 h, (b) SR+SA 4 h and (c) SA 24 h. 21
4.5 KAM maps that shows local distortion of the lattice within grains for samples from print B (a) SA 4 h, (b) SR+SA 4 h and (c) SA 24 h. . . 21
4.6 LOM images of etched samples produced from VIGA powder at 300 W laser power: (a) 10 mm cube in the SR (900 °C for 30 min) condition, (b) 10 mm cube in the SR+SA(1200 °C for 4 h) condition, (c) 2 mm thick thin wall in the SR condition and (d) 2 mm thick thin wall in the SR+SA condition. 22
4.7 Optical microscope images of etched samples in the SA condition (1200 °C for 4 h) printed using GA powder: (a) 10 mm cube and (b) 0.5 mm thick thin wall. 23
4.8 Average deviation of the grain counting script relative to EBSD-derived reference data. 23
4.9 Histogram of equivalent diameter of grains in samples in both print A and B obtained by EBSD. 24

List of Tables

3.1 Typical chemical composition of VIGA nuclear grade powder used in this study, supplied by the manufacturer. 11
3.2 Samples included in print A with stress relieved (SR) at 900 °C for 30 min and solution annealing (SA) at 1200 °C for 4 h. 12
3.3 Typical chemical composition of GA powder used in this study, supplied by the manufacturer. 12
3.4 Samples included in print B with as-built (AB), SR at 900 °C for 30 min, SA at 1200 °C for 4 h and SA extended at 1200 °C for 24 h. . 12

4.1 Grain size measurements performed by Frangi filter for samples in Fig. 4.1 18
4.2 Obtained from EBSD measurements for print A, the mean orientation spread represents the average crystallographic distortion within a grain relative to its mean orientation. $<2°$ is considered recrystallized for a grain. 19
4.3 GB distribution from Fig. 4.4. 21
4.4 Obtained from EBSD measurements for print B, the mean orientation spread represents the average crystallographic distortion within a grain relative to its mean orientation. $<2°$ is considered recrystallized for a grain. 22
4.5 Median equivalent diameter of selected samples, obtained by EBSD measurements. 24
4.6 Levels of oxygen and nitrogen in powder and printed part measured by combustion. 24

1 Introduction

Rapid development in recent years has made additive manufacturing (AM) a viable alternative for production of a variety of different types of items, often matching and sometimes exceeding the properties of conventionally produced parts [1]. Among the available AM techniques, powder bed fusion – laser beam (PBF-LB) is particularly well established for austenitic stainless steels in industries such as automotive and aerospace due to its ability to produce net-near-shape parts with complex geometries and minimal material waste [2].

The nuclear industry presents a compelling use case for PBF-LB. Components within nuclear power plants are subject to stringent material qualification requirements, and replacement parts are not always readily available, creating a trade-off between maintaining costly inventory and risking extended downtime [3]. The International Atomic Energy Agency estimated in 2019 that a 1 GW plant loses approximately €1.2 million in revenue per 24 h of downtime [4]. On-demand fabrication of spare parts by PBF-LB could significantly reduce both lead times and cost compared to conventional manufacturing [5, 6]. Among candidate materials, 316L stainless steel is particularly relevant due to its corrosion resistance, mechanical performance in low to medium temperature ranges and established history in nuclear service [7].

However, PBF-LB produced 316L deviates significantly from its wrought counterpart. The rapid heating and cooling cycles inherent to the build process produce a highly anisotropic, non-equilibrium microstructure characterized by columnar grains, elevated residual stresses and a high density of geometrically necessary dislocations (GND) [8]. These features compromise performance in the as-built (AB) state and must be addressed through post-process heat treatment before the component can meet service requirements [7]. The recrystallization behavior of PBF-LB 316L during heat treatment is sensitive to the combined effects of powder feedstock, process parameters and thermal history, and remains insufficiently understood [9, 10]. In particular, the role of powder type and the differences in inclusion content between two conventional atomization routes, gas atomized (GA) and vacuum induction gas atomized (VIGA), has received limited attention. Furthermore, grain boundary engineering (GBE), which aims to manipulate the grain boundary (GB) structure by, inter alia, increasing the fraction of low-energy $\Sigma 3$ twin boundaries to improve resistance to corrosion and stress corrosion cracking, has only recently begun to be explored in the context of AM-produced near-net-shape components, where conventional deformation based GBE routes are not applicable [9, 11, 12].

This master's thesis work was conducted in collaboration with Vattenfall within the frame of project roBust post-pRocessing of AdditiVEly manufactured components (BRAVE) as part of Materials Chemistry (MPMCN) and aims to address the following research questions:

- How is the microstructural evolution during heat treatment of PBF-LB 316L SS influenced by process parameters and powder feedstock?
- Does a stress relief cycle affect the recrystallization during the subsequent solution annealing of PBF-LB 316L SS?
- Does part geometry significantly influence recrystallization behavior of PBF-LB 316L SS?
- Can a custom image analysis method based on light optical microscopy provide grain size measurements consistent with EBSD for PBF-LB microstructures?

2

Theory

2.1 Additive manufacturing

Additive manufacturing (AM), commonly referred to as 3D printing, relies on building a product by adding material layer by layer, unlike subtractive manufacturing which involves the removing of material from an oversized starting block to achieve its final shape. AM can be used with a wide variety of materials with a few different techniques such as plastic extrusion and powder bed fusion. [1]

AM in general has the capability to produce parts of complex geometries that are not possible by conventional manufacturing (CM) with high customizability, while producing almost no waste. It can revolutionize entire supply chains as the time from prototype development to final component can be significantly reduced [2]. Metal components produced by AM can however be affected by; higher than optimal porosity, poor surface finish and residual stresses, which influence mechanical properties including strength, corrosion resistance and fatigue performance. There are several strategies to address this such as tuning the production parameters and post-processing [13] and with recent development, fatigue performance of AM produced items are comparable to CM for some alloys [14].

2.1.1 Powder Bed Fusion - Laser Beam (PBF-LB)

Powder Bed Fusion – Laser Beam (PBF-LB) is an advanced AM method for printing alloys that involves layering powder on the bed and with laser selectively melting and fusing the powder in the required pattern, the bed is lowered by one layer and new powder is coated on top and the process is repeated. Perpendicular to the recoater direction, is a constant flow of inert shielding gas [2]. This can be viewed in Fig. 2.1. The rapid heating and cooling in multiple cycles will often promote an anisotropic metastable microstructure. Printing parameters (Section 2.1.3) such as scan speed, laser power and scanning strategy such as hatch spacing (the length between two scan lines) are examples of parameters that can be tuned to alter the microstructure [9, 11, 15–17]. To further refine the microstructure after printing, heat treatment (HT) is common practice [18–20].

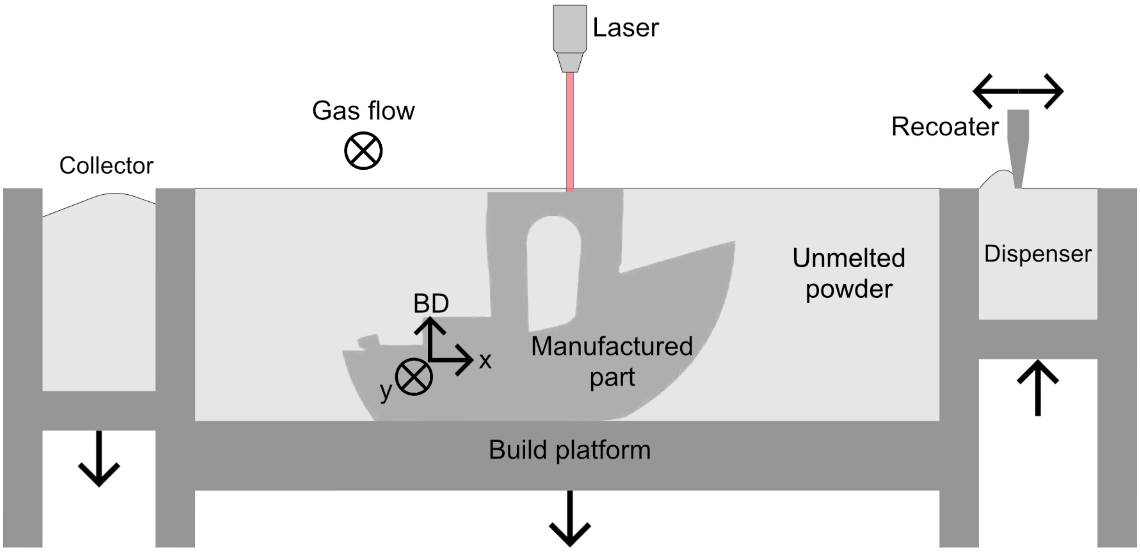

Figure 2.1: Schematic illustration of a generic PBF-LB system. After each build cycle, the build platform is lowered by one layer height. New powder is raised from the dispenser and spread across the build area by the recoater. Excess powder is captured by the overflow collector, and the laser selectively melts the newly deposited layer. The process is repeated layer by layer until the print is complete.

2.1.2 Powder

AM processes based on PBF-LB rely on layers of alloy powder being put down in thin, even layers to maintain consistency and integrity when melted by the laser. As a result, the characteristics of the powder feedstock are important for ensuring print quality. Powder geometry influences spreadability and packing density, while the chemical composition of the powder affects the composition and properties of the final product. Both gas atomized (GA) and vacuum induction gas atomized (VIGA) powders are manufactured by atomizing a stream of molten alloy using high pressure inert gas jets, producing uniform near spherical particles. The production differs slightly in melting, where GA is melted in open air before atomization, VIGA is melted under a vacuum, both exhibit good flowability and packing density, and therefore high printability [21, 22]. Unmelted and overflow powder (see Fig. 2.1) is no longer regarded virgin after first use but can be reused. Despite the care taken to keep powder in an inert atmosphere at most times, the powder gradually deteriorates slightly and cannot be reused indefinitely due to a build-up of surface oxides [23].

2.1.3 PBF-LB of 316L SS

316L stainless steel is an alloy widely processed in PBF-LB, owing to its good printability, well documented mechanical properties and broad industrial relevance [15]. Its corrosion resistance and mechanical properties make it particularly attractive for nuclear applications, as discussed in the introduction, where the ability to produce near-net-shape components on demand presents a compelling alternative to conventional manufacturing routes [3, 5].

The microstructure of PBF-LB produced 316L deviates substantially from its wrought counterpart. In conventionally produced 316L, thermomechanical processing and solution annealing yield a recrystallized grain structure with low residual stresses, though grain morphology and crystallographic texture vary with processing route, ranging from equiaxed with near-random texture to elongated grains with a clear texture [24]. PBF-LB produces a highly anisotropic, non-equilibrium microstructure as a consequent of the rapid heating and cooling cycles inherent to the process [7]. Solidification occurs epitaxially along the build direction, following the steep thermal gradient, resulting in columnar grains that can span multiple melt pool layers [9, 11]. Within these grains, a characteristic cellular substructure forms, outlined by dislocation networks and decorated with nanoscale oxide and silicate inclusions segregated from the melt [25]. The rapid heating and cooling also promotes a high density of geometrically necessary dislocations (GND) and significant residual stresses in the as-built (AB) state [13, 26], both of which influence the response to heat treatment. These features collectively result in mechanical properties that differs from wrought 316L [19].

The AB microstructure is sensitive to the processing parameters used during printing. Laser power, scan speed and hatch spacing collectively determine the volumetric energy density delivered to the powder bed, which in turn governs melt pool geometry, solidification rate and the resulting grain morphology [11, 15]. Higher laser power or lower scan speeds produce deeper melt pools and trap gases (so-called keyhole porosity) and produce more pronounced epitaxial grain growth, while insufficient energy input can lead to lack-of-fusion (LoF) pores bonding between the layers becomes incomplete [13]. Despite the extensive literature on PBF-LB 316L, the combined influence of process parameters, powder feedstock and thermal history remains insufficiently understood [8, 27]

2.2 Heat treatment (HT)

HT is a fundamental part of the post processing of virtually any metallic part to tailor the microstructure and properties trough controlled thermal cycles. By adjusting temperature and holding time, internal stresses can be relaxed, and recrystallization and grain growth can be promoted. HT leads to changes in grain boundary characteristics and microstructure which directly influence mechanical properties, corrosion resistance and thermal stability [28]. For PBF-LB produced parts HT is particularly important due to in AB state is a non-equilibrium anisotropic state with high level of residual stresses [7, 29].

This forms the basis of GBE in AM, which aims to control the changes in microstructure to achieve the required result.

2.2.1 Grain Boundary Engineering (GBE)

GBE refers to the deliberate manipulation of grain boundary (GB) structure, conventionally through complex thermal and deformation cycles, to achieve recrystallization and improve the properties of the material [9, 11, 12]. Unwanted characteristics of GBs in polycrystalline materials can lead to deterioration in multiple properties, including susceptibility to intergranular corrosion, stress corrosion cracking, stress localization and creep-induced GB fracture, particularly when high angle random GBs are sensitized [30]. As PBF-LB produces a near-net-shaped product, conventional GBE by deformation cannot be applied without compromising the design, therefore, new approaches are being developed. Challenges that these poses include achieving satisfactory recrystallization and managing solute interactions. The high energy and strain metastable microstructure of the PBF-LB prints is believed to lower the thermal stability, thereby promoting recrystallization without deformation [9].

Dislocations can be broadly classified into statistically stored dislocations (SSD) and geometrically necessary dislocations (GND). SSDs are randomly distributed within the material and arise from homogeneous plastic deformation and does not produce a net lattice curvature. While GNDs arise from non-uniform plastic deformation or rapid local heating and cooling. GND accommodate strain gradients within the material and are required to maintain lattice continuity [31]. In AM austenitic steel, GND account for most of the dislocations [19, 32]. By adjusting the printing parameters, the microstructure can be locally controlled, enabling recrystallization to occur in specific regions after HT while other areas remain unaffected. This is achieved by introducing a high density of GND in targeted areas, which reduces the thermal stability in that area and thus promotes recrystallization locally. The GNDs can be introduced by increasing the number of thermal cycles the material goes through during a print [9, 11, 17].

2.2.2 Strengthening mechanisms

There are multiple strengthening mechanisms in austenitic stainless steels, which arise from interactions that hinder dislocation movement. Since plastic deformation mainly occurs through the movement of dislocations, hindrance of this results in increased yield strength.

2.2.2.1 Grain boundary strengthening

One important mechanism is grain boundary strengthening described by the Hall–Petch relationship, which relates grain size to material strength. GBs can be categorized as low angle ($\leq 10°$) and high angle ($> 10°$) which is defined by the misorientation of the two grains that meet and form the GB. Low angle GBs consists mostly of arrays of edge dislocations while high angle GB require a more complex combination of dislocations and acts as obstacles to dislocation motion, resulting in accumulation of dislocations at GBs [33]. Hall–Petch relation is explained by:

$$\sigma_y = \sigma_0 + k_1 D_{GB}^{-1/2} \tag{2.1}$$

where D_{GB} is the grain size, σ_y is the yield stress related to the grain size and σ_0 and k_1 are constant. σ_0 is a friction stress caused by solutes but not dislocations [34]. In PBF-LB produced 316L, the fine and anisotropic grain structure contributes to grain boundary strengthening, however recrystallization and grain growth during heat treatment can coarsen the grain structure and thereby reduce the contribution of this mechanism [19].

2.2.2.2 Solid solution strengthening

Solid solution strengthening in 316L arises from the presence of alloying elements, both substitutional and interstitial. Chromium, nickel and molybdenum are dissolved in the austenitic iron matrix while interstitial solutes situate between the atoms that make up the lattice. The increase in strength comes from the difference in size between the solute atoms and the solvent iron atoms, which creates local lattice distortions and associated stress fields that impede dislocation motion (as seen in Fig. 2.2 (a)) [35].

2.2.2.3 Dislocation strengthening

Dislocation strengthening arises from interaction between moving dislocations and existing dislocation structures within the material. In 316L SS produced by PBF-LB the rapid heating and cooling leads to a high density of dislocations arranged in networks, cell structures, and entangled configurations. These dislocation structures act as strong obstacles to further dislocation motion, increasing strength of the material [36].

2.2.2.4 Orowan strengthening

Orowan strengthening occurs when dislocation lines encounter particles or inclusions within the bulk material. Since these obstacles are non-shareable, the dislocations cannot pass through but instead bow around the particles, leaving behind dislocation loops. This process requires an increased applied stress and thereby contributes to strengthening [35]. An illustration of this can be seen in Fig. 2.2 (d). Finely dispersed particles enhance the Orowan strengthening effect, as reduced spacing between obstacles increases the resistance to dislocation motion. However, inclusions tend to coarsen and agglomerate due to Ostwald ripening, which increases the interparticle spacing and reduces the strengthening effect [19, 21]. This coarsening is promoted by slow cooling after HT [7].

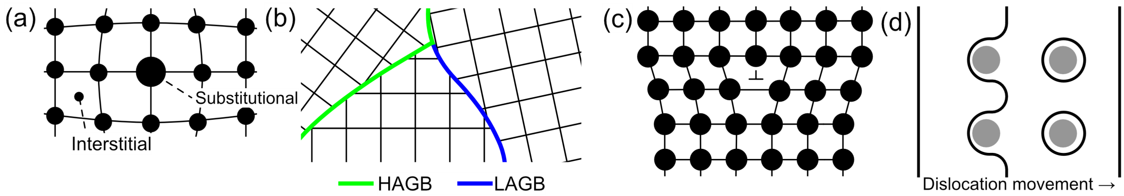

Figure 2.2: Strengthening mechanisms (a) solid solution, (b) GB strengthening with high angle grain boundary (HAGB) in green and low angle grain boundary (LAGB) in blue, (c) edge dislocation that acts as dislocation strengthening and (d) dislocation line being hindered by Orowan strengthening. Inspired by [35].

These strengthening mechanisms depend on the thermal history and are not independent of one another but are instead interrelated. However, as shown by Li et al., their contributions can be considered approximately additive [19]. By estimating the strengthening effect from each mechanism and summing them, a reasonable approximation of the material's overall strength can be obtained [19].

2.2.3 Annealing twins

Annealing twins are a common microstructural feature in FCC materials with low stacking fault energy, including austenitic stainless steels such as 316L. In 316L SS, the proportion of twin boundaries in conventionally solution annealed material typically exceeds 30 %. Their formation is generally contributed to growth accidents during GB migration, wherein a local change in stacking sequence occurs as atoms are incorporated into the advancing crystal lattice. For this mechanism to operate, the GB must migrate in the opposite direction to its center of curvature, a condition that can arise during recrystallization but is less typical during normal grain growth. The precise formation mechanism of annealing twins remains an active area of research, with multiple models proposed [37]. Annealing twins are defined by a specific crystallographic orientation relationship between the parent grain and the twinned region, corresponding to a $\Sigma3$ coincidence site lattice (CSL) boundary with a misorientation of 60 ° about the $\langle 111 \rangle$ axis [38]. During the beginning of the recrystallization regime, twin formation is favored by high stored strain within the material [39]. Annealing twins can also influence mechanical properties and corrosion resistance. $\Sigma3$ twin boundaries on $\{111\}$ planes are fully coherent interfaces with significantly lower interfacial energy than other HAGB. In 316L, samples with a high fraction of CSL boundaries exhibit sustained strain hardening and enhanced ductility, partially attributed to a higher barrier effect of twins [40].

2.2.4 Second phase particles

The impact of second phase particles on recrystallization is complex, as multiple mechanisms interact simultaneously during solution annealing [41]. For polycrystalline materials, GB migration is the primary mechanism by which recrystallization and grain growth occur. The driving force for this migration is the reduction in total GB energy associated with increasing mean grain size. However, when second phase particles are present within the microstructure, they exert a retarding force on migrating GBs, a phenomenon first rationalized by Smith [42] and later detailed by Zener [43]. The physical basis of this drag is that a GB intersecting a particle locally reduces the boundary area, and thereby its energy. Detaching from the particle requires recreating that boundary area, imposing an energetic penalty that impedes further boundary motion. This mechanism is known as Smith-Zener pinning [44]. In PBF-LB produced 316L, the rapid melting and solidification of successive powder layers promotes the formation of a high density of nanoscale oxide and silicate inclusions, distributed both within grains and along grain boundaries [45], which act as Smith-Zener pinning agents and contribute to the sluggish recrystallization kinetics observed in PBF-LB 316L compared to its wrought counterpart [8].

Conversely, coarse second phase particles exceeding a critical size of approximately 1 µm can promote recrystallization through particle stimulated nucleation (PSN) [46]. In PSN, the local deformation zone surrounding a sufficiently large particle contains a high dislocation density and steep crystallographic orientation gradients, providing the thermodynamic and kinetic conditions necessary for nucleation of a new grain at the particle interface. This accelerates recrystallization and tends to produce a finer grain size and a near-random texture compared to recrystallization by other nucleation mechanisms [41].

In practice, both mechanisms may operate concurrently during solution annealing of PBF-LB 316L. Fine nanoparticles pin grain boundaries and retard recrystallization, while simultaneously coarsening via Ostwald ripening as the annealing temperature is maintained. As particles grow, the Smith-Zener pinning pressure decreases and should any particles exceed the PSN threshold, nucleation at those sites becomes possible. The net recrystallization behavior is therefore sensitive to the initial particle size distribution [8].

2.2.5 Stress relieving (SR)

Stress relieving is a heat treatment process aimed at reducing residual internal stresses while preserving the overall microstructure. In PBF-LB-produced parts, significant residual stresses develop in the as-built condition due to the steep thermal gradients inherent to the process, resulting in an anisotropic and metastable microstructure. When left unmitigated, these stresses may contribute to dimensional instability or cracking [13, 29]. SR of austenitic stainless steels is typically performed either below 480°C or in the range of 900–1120°C, with cooling by furnace cooling, air cooling or water quenching depending on part geometry and distortion sensitivity [47, 48]. Prolonged exposure in the intermediate range of 480–900°C is generally not recommended as it carries a risk of grain boundary carbide precipitation and sensitization, though susceptibility is strongly dependent on carbon content and time at temperature, low carbon grades like 316L are generally not susceptible to carbide precipitation [47, 49].

2.2.6 Solution annealing (SA)

Solution annealing is a HT process commonly applied to austenitic stainless steels such as 316L to modify the microstructure and restore ductility. The process involves heating the material to 0.75-0.9 T_m, where the alloying elements fully dissolve in the austenitic matrix and particle inclusions are distributed. Followed by quenching to prevent the alloying elements migrating to GBs and particle inclusions to cluster, thus retaining the solid solution and Orowan strengthening mechanisms and suppresses carbide formation [7]. Conventional 316L is solution annealed at 1093°C with soaking times depending on part thickness followed by water quenching, or if the part is especially prone to distortion polymer quenching [48].

The theoretical framework outlined in Chapter 2 forms the basis for the experimental design in this work. While the microstructural response of PBF-LB 316L to heat treatment has received increasing attention, the governing parameters of recrystallization behavior remain an active area of research. Two powder atomization routes, heat treatment conditions, laser power and part geometry were therefore selected to systematically investigate these effects in the context of near-net-shape components.

3
Methods

3.1 Prints

Two separate print campaigns were investigated. Print A was used to evaluate the influence of process parameters and part geometry in material produced from VIGA powder. Based on the observations from Print A, a second print campaign (Print B) was designed to investigate the influence of heat treatment, powder feedstock and part geometry using GA powder while maintaining constant process parameters.

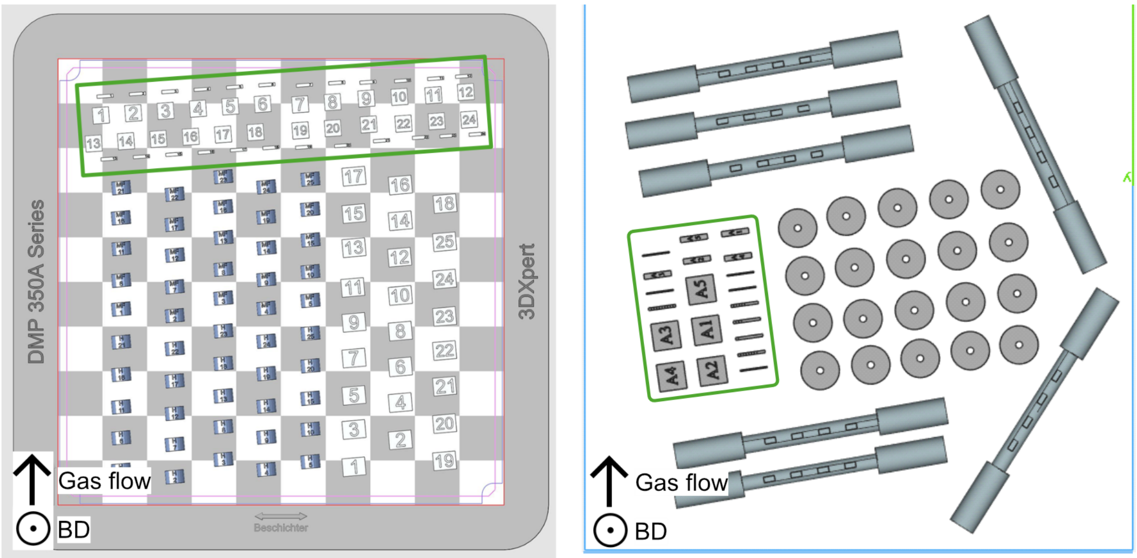

(a) (b)

Figure 3.1: Build plates of the two prints, the green boundaries indicate the samples included in this study. (a) print A, printed using VIGA powder by external manufacturer and (b) print B, printed using GA powder in-house.

3.1.1 Print A

Table 3.1: Typical chemical composition of VIGA nuclear grade powder used in this study, supplied by Höganäs AB [50].

316L NG 15-63 µm VIGA					
Element	Cr	Ni	Mo	Co	Fe
Content [wt. %]	17.5	12	2.6	0.01	Balance

Print A was printed using VIGA powder (Table 3.1) in *3DSystems DMP Flex 350 (beam ø = 62 µm)* (Fig. 3.1a), 10 mm cubes and 2x10x10 mm thin walls were included. The printed parts were stress relieved at 900 °C for 30 min under vacuum followed by slow cooling at a rate of 1.5 °C/min prior to being dismounted from the build plate. If solution annealed (1200 °C for 4 h), this treatment was also carried out under vacuum. The laser power was varied from 200 W to 350 W between the different objects during the print. For studies other than process parameter study, 300 W laser power was used as standard parameter since this is by the manufacturer recommended setting. These samples were printed and heat treated by an external manufacturer and were received in their respective conditions, as shown in Table 3.2.

Table 3.2: Samples included in print A with stress relieved (SR) at 900 °C for 30 min and solution annealing (SA) at 1200 °C for 4 h.

Sample group	HT condition	Laser power [W]
Print A	SR	200
Print A	SR	300
Print A	SR	350
Print A	SR+SA	200
Print A	SR+SA	300
Print A	SR+SA	350

3.1.2 Print B

Table 3.3: Typical chemical composition of GA powder used in this study, supplied by Höganäs AB [50].

316L 20-53 µm GA								
Element	Cr	Ni	Mo	Mn	Si	C	O	Fe
Content [wt. %]	17	12	2.5	1.5	0.8	0.01	0.06	Balance

Print B was produced using GA powder (Table 3.3) in the *EOSM290 (beam ø =80 µm)* system (Fig. 3.1b). The printed geometries included 10 mm cubes and 10×10 mm square thin walls with thicknesses of 2 mm, 1 mm, and 0.5 mm.

Table 3.4: Samples included in print B with as-built (AB), SR at 900 °C for 30 min, SA at 1200 °C for 4 h and SA extended at 1200 °C for 24 h.

Sample group	HT condition
Print B	AB
Print B	SR
Print B	SR+SA
Print B	SA
Print B	SA extended

The heat treatment scheme (Table 3.4) was based on [25] and was further developed to investigate the recrystallization behavior of parts produced by PBF-LB. Process parameters used in this print was by the manufacturer recommended standard settings. Three HT conditions were employed: stress relieving (SR), performed at 900 °C for 30 min followed by cooling at 1.5 °C/min; solution annealing (SA) at 1200 °C with varying holding times followed by water quenching; and a combined SR+SA treatment, where specimens were first stress relieved under the same SR conditions and subsequently solution annealed as described above.

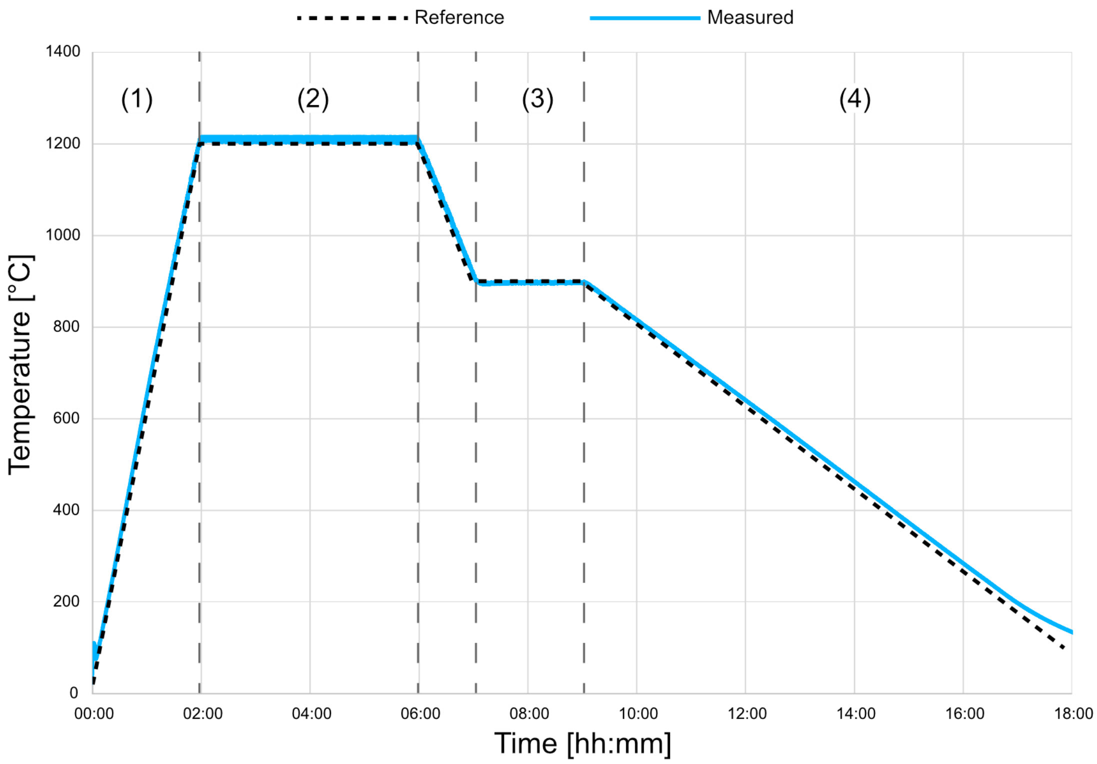

Figure 3.2: Tube furnace with argon atmosphere calibration cycle over the thermally relevant regime. The dotted line represents the reference temperature and the solid blue line the measured temperature. (1) Heating from RT to 1200 °C at 10 °C/min, (2) isothermal hold at 1200 °C, (3) isothermal hold at 900 °C, and (4) cooling from 900 °C to RT at 1.5 °C/min.

Samples printed using GA powder were dismounted prior to any heat treatment. The heat treatment was carried out in a tube furnace under argon atmosphere Since surface effects were not investigated, the different atmospheres were considered comparable. Calibration of the tube furnace (Fig. 3.2) was performed using a class 1 IEC 60584-2 certified thermocouple probe to ensure comparability with the heat treatment schemes applied in this study.

3.2 Characterization

Microstructural evolution was characterized primarily using light optical microscopy (LOM) and quantitative image analysis, with selected samples additionally characterized by electron backscatter diffraction (EBSD). LOM was selected as the primary characterization tool due to its accessibility and significantly lower cost and time requirements compared to EBSD, making it practical for screening larger sample sets.

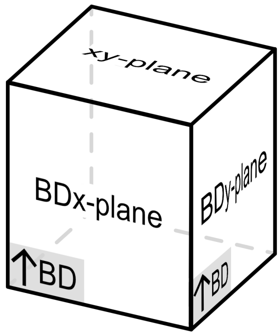

Figure 3.3: Schematic illustration of the sample orientation used in this work, showing the xy-plane, BDx-plane, and BDy-plane relative to the build direction (BD) in the PBF-LB process.

The planes of the printed component are visualized in Fig. 3.3, for the purpose of this study x and y direction are not differentiated hence BDx- and BDy-plane are mentioned as BD-plane due to their similarities (for further context see Fig. 2.1).

Prior to LOM, samples were prepared by cutting with *BUEHLER IsoMet High Speed Pro Precision* to reveal the bulk material and mounted in Bakelite by *Struers Citopress-20*, ground flat and polished to 1 µm diamond suspension by *Struers TegraPol-31*. To reveal the microstructure under LOM, the samples were etched in 10% oxalic acid using a platinum counter electrode and applied potential of 3 V. Samples were viewed and photographed using *ZEISS Axioscope 7* LOM. For EBSD, the samples were further polished with OPU and OPS.

3.2.1 Image analysis

Grain segmentation was performed using a custom Python image analysis script, developed for LOM images of acid etched 316L SS. Images were enhanced by contrast-limited adaptive histogram equalisation (CLAHE, clip limit 0.03) to normalize local intensity variations. GBs were detected using the Frangi vesselness filter applied at scales of 1-7 pixels, which responds strongly to narrow, elongated morphology of GBs. The resulting Frangi response map was thresholded at the 83rd percentile and the resulting binary mask was skeletonized. Endpoints caused by gaps in the network created by photographic or etching defects and junctions that were suppressed by Frangi due to their blob-like appearance were reconnected within a 20 pixel radius. Grains touching the image border were excluded in accordance with

ASTM E112, regions smaller than 30 px^2 or with an aspect ratio greater than 100 were excluded to remove artifacts.

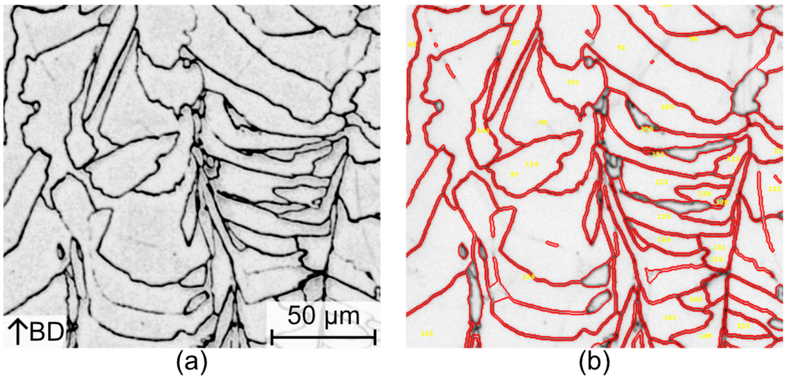

Figure 3.4: Etched sample in BD-plane analyzed with Frangi mask (a) LOM image of etched sample and (b) same image with Frangi filter overlay.

For validation, an overlay of the segmented boundaries on the original image (as seen in Fig. 3.4), along with thumbnails of individual grains, was generated for visual inspection. Quantitative metrics, including grain area, major and minor axis, Feret diameter length and orientation and additional shape descriptors, were computed for each grain in both pixel and physical units.

3.2.2 Electron backscatter diffraction (EBSD)

EBSD analysis was performed to evaluate the degree of recrystallization, GB characteristics and validate grain segmentation obtained by image analysis. Measurements were conducted on the BD-plane using *Zeiss Gemini 450* at an acceleration voltage of 20 kV. Samples were tilted to 70° relative to the incident electron beam during acquisition. EBSD maps were gathered at 73× magnification, using a step size of 2 µm. Each scan covered an area of 1550×1162 µm.

GB character was classified by misorientation angle into low angle grain boundaries (LAGB, 2–10°) and high angle grain boundaries (HAGB, >10°). Annealing twin boundaries were identified as Σ3 CSL boundaries corresponding to a misorientation of 60° about the ⟨111⟩ axis [25]. The degree of recrystallization was assessed using the mean orientation spread (MOS), where grains with MOS below 2° were considered recrystallized [8]. Local lattice distortion within grains was further evaluated using kernel average misorientation (KAM) maps, which provide a spatially resolved indication of residual strain and geometrically necessary dislocation density.

4

Results

4.1 Influence of process parameters on microstructure after heat treatment

To determine the impact of melt pool geometry/shape on the microstructure evolution during heat treatment, selected samples were etched and examined by LOM.

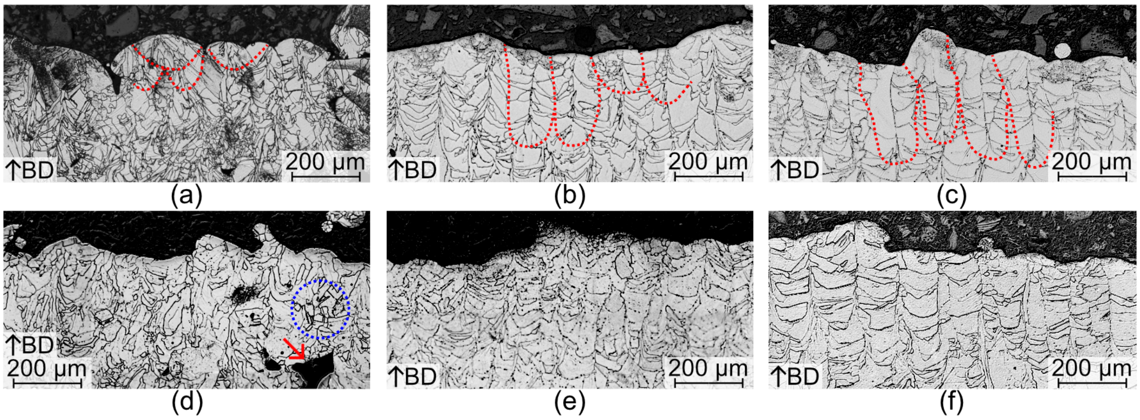

Figure 4.1: Optical microscope images of etched VIGA cubes, printed with varying laser power in SR (900 °C 30 min) and SR+SA (900 °C 30 min and 1200 °C 4 h) condition. (a) 200 W SR, (b) 300 W SR, (c) 350 W SR, (d) 200 W SR+SA red arrow pointing out LoF pore and recrystallized area circled in blue, (e) 300 W SR+SA and (f) 350 W SR+SA.

In Fig. 4.1 a-c the traces of melt pools boundaries are still visible after the stress relieve. At 200 W laser power (Fig. 4.1a), LoF pores (marked with red arrow in Fig. 4.1d) are observed, consistent with the shallow melt pools not providing sufficient bonding with previous layers. The microstructure consists of fine, irregular grains orientated towards the melt pool center lines. At 300 W (Fig. 4.1b), melt pools are significantly deeper than those observed at 200 W. Increased laser power to 350 W results in slightly deeper and more keyhole-like melt pools. The grains remain irregular but larger than those formed at 200 W. Grains clearly converge toward melt pool center lines, forming a melt pool-like pattern offset from the actual melt pool.

After solution annealing (Fig. 4.1d-f) at 1200 °C for 4 h following stress relief, the melt pool boundaries are no longer visible, indicating complete dissolution of the original melt pool structure. However, the microstructure remains largely unchanged, except for occasional recrystallized grains approximately 150 µm in size. The most significant microstructural changes are observed in the 200 W sample (Fig. 4.1d), where partial recrystallization occurs (circled in blue and characterized by the presence of annealing twins). Nevertheless, the grains remain irregular, and the overall degree of recrystallization is limited.

This is further supported by grain size measurements obtained using the Frangi vesselness filter (Table 4.1), where samples produced at lower laser power exhibited smaller grain sizes and a more pronounced response to solution annealing. In contrast, the samples produced at 300 W and 350 W showed smaller differences in grain size after solution annealing.

Table 4.1: Grain size measurements performed by Frangi filter for samples in Fig. 4.1

Laser power [W]	200				300				350			
Condition	SR		SR+HT		SR		SR+HT		SR		SR+HT	
Plane	BD	xy	BD	xy	BD	xy	BD	xy	BD	xy	BD	xy
Median equivalent diameter [µm]	15.42	14.76	18.89	18.17	22.37	21.34	18.09	17.64	19.06	19.45	18.69	18.24

4.2 Influence of heat treatment

Investigations were carried out to determine how the microstructure of 316L stainless steel produced by PBF-LB is affected by heat treatments, including combinations of stress relieving and solution annealing.

4.2.1 Print A using VIGA powder

For a closer look at the effect of HT on the samples printed using VIGA powder, only the 300 W laser power is shown as this is considered the standard setting for that printer.

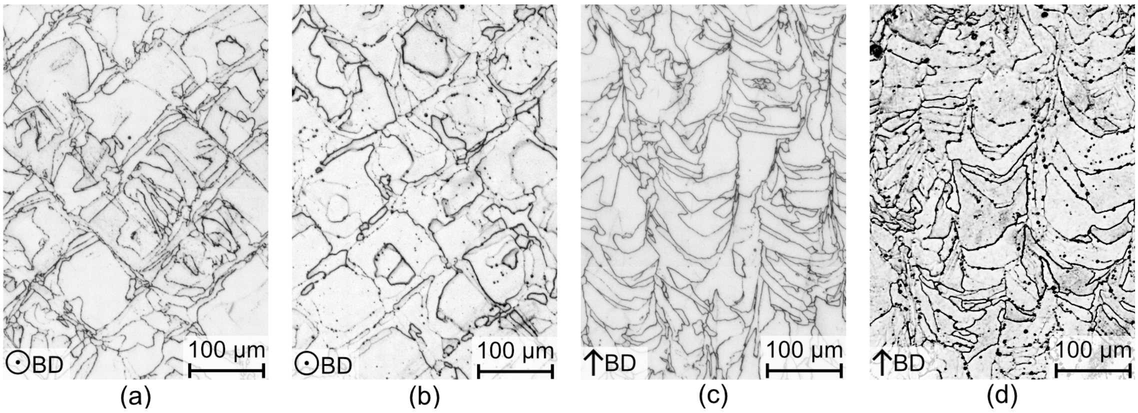

Figure 4.2: Optical microscope images of etched samples printed using VIGA powder. xy-plane: (a) SR 900 °C 30 min and (b) SR 900 °C 30 min and SA 1200 °C 4 h. BD-plane: (c) SR 900 °C 30 min and (d) SR 900 °C 30 min and SA 1200 °C 4 h.

Figure 4.2a shows the xy-plane of the stress relieved sample which exhibits a checkerboard pattern of equiaxed grains formed during scanning of the laser with the higher density of GBs indicating the center of the scan line resulting from cooling of the melt pool. The BD plane (Fig. 4.2c), the grain structure shows a characteristic fish scale pattern of anisotropic columnar grains formed during solidification in the build process. In SA condition (Fig. 4.2b in xy-plane and d in BD plane), the original grain structure is largely maintained, with no significant recrystallization observed, as further evidenced by mean orientation spread (MOS) shown in Table 4.2. In addition, particles that is mainly situated along the grain boundaries can be seen in the SA condition.

Table 4.2: Obtained from EBSD measurements for print A, the mean orientation spread represents the average crystallographic distortion within a grain relative to its mean orientation. <2° is considered recrystallized for a grain.

Condition	SR+SA 4 h
Mean orientation spread <2° [%]	60.9

4.2.2 Print B using GA powder

Samples printed by the EOS M290 using GA powder were subjected to an additional heat treatment scheme to further examine the potential impact of a stress relief cycle prior to solution annealing. All samples were printed with standard parameters for the printer.

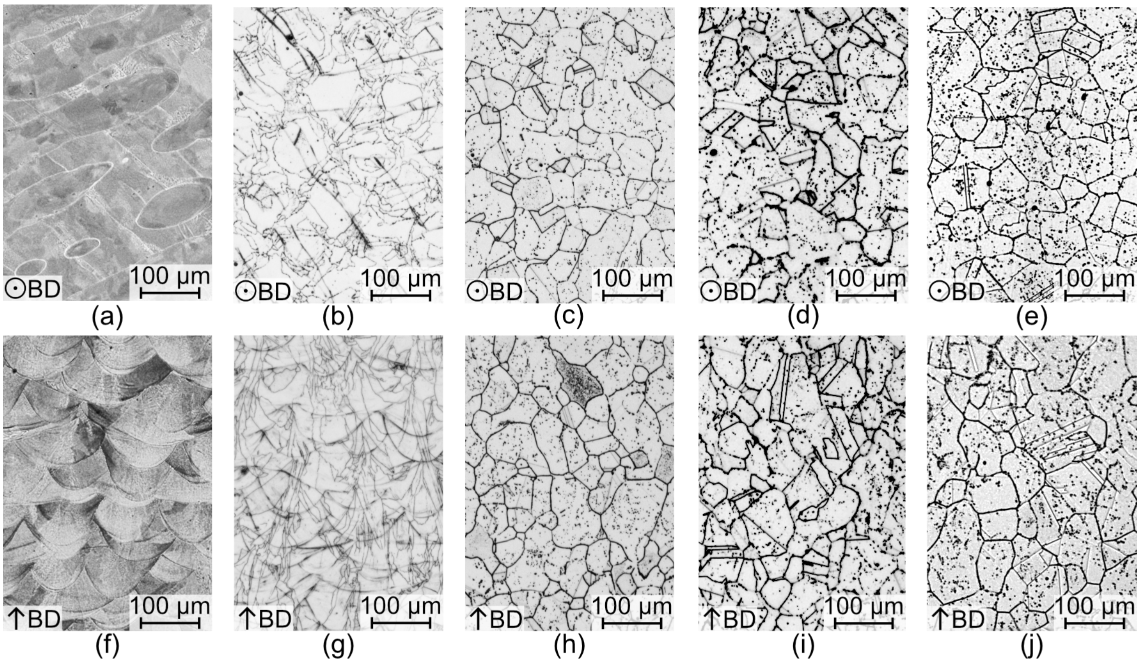

Figure 4.3: Optical microscope images of etched samples printed using GA powder. xy-plane: (a) AB, (b) SR 900 °C 30 min, (c) SR 900 °C 30 min and SA 1200 °C 4 h, (d) SA 1200 °C 4 h and (e) SA 1200 °C 24 h. BD-plane: (f) AB, (g) SR 900 °C 30 min, (h) SR 900 °C 30 min and SA 1200 °C 4 h, (i) SA 1200 °C 4 h and (j) SA 1200 °C 24 h.

Figure 4.3a shows the AB condition where clear scan lines are visible in the xy-plane. Following stress relieving (Fig. 4.3b) the checkerboard pattern of the equiaxed grains is revealed, also showing traces of melt pool boundaries. In the BD, AB (Fig. 4.3f) shows overlapping melt pools and after SR (Fig. 4.3g) the melt pools are still visible but also epitaxial columnar grains following the thermal gradient.

A solution annealing following a stress relief (Fig. 4.3c in xy-plane and h in BD plane) appears to dissolve the original microstructure and produce a recrystallized grain structure with little resemblance to the initial condition. Annealing twins can be found throughout the sample, although the Σ3 GB are less susceptible to etching and therefore may appear faint. Solution annealed for 4 h (Fig. 4.3d in xy-plane and i in BD plane) and 24 h (Fig. 4.3e in xy-plane and j in BD-plane) both exhibit a similar grain structure to Fig. 4.3c and h without any visible traces of the original microstructure, however the density of annealing twins appear higher after 24 h of annealing.

All samples produced using GA powder and subjected to solution annealing exhibited a high density of particulates, located not only along the grain boundaries but also within the grains.

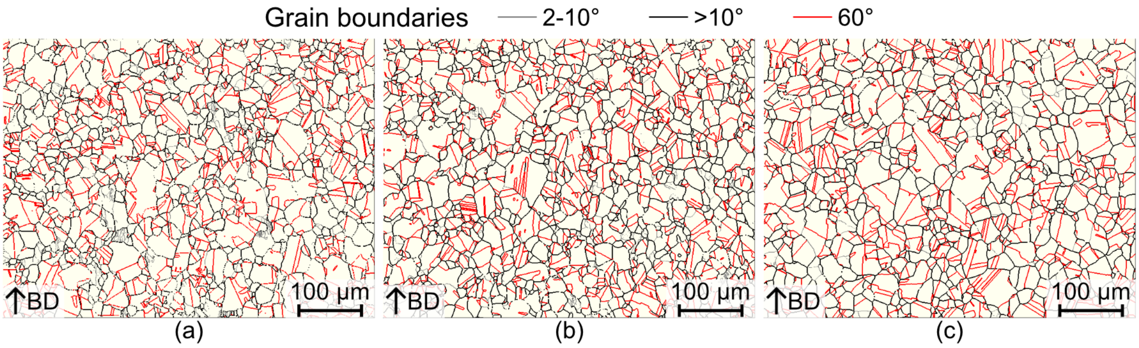

Figure 4.4: EBSD acquired image of grain boundaries in samples from print B (a) SA 4 h, (b) SR+SA 4 h and (c) SA 24 h.

Further highlighting the extent of recrystallization, Fig. 4.4 shows the categorized GB characteristics for the solution annealed GA samples defined by number of pixels that make up the GB. LAGBs (2–10°) are associated with retained dislocation substructure from the as-built condition, while HAGBs (>10°) are characteristic of recrystallized grain structures. The fraction of Σ3 boundaries reflects the extent of annealing twin formation during solution annealing. Tabulated values are given in Table 4.3 and show a similar twin boundary fraction between the two SA samples and reduced for the SR+SA sample. Total HAGB fraction is highest in SA 24 h and lowest for SA 4 h.

Table 4.3: GB distribution from Fig. 4.4.

Condition	SA 4 h	SR+SA 4 h	SA 24h
Grain boundaries 2–10° [%]	9.1	6.7	3.8
Grain boundaries >10° [%]	90.9	93.3	96.2
Annealing twin boundary (60°) [%]	43.8	39.7	44.3

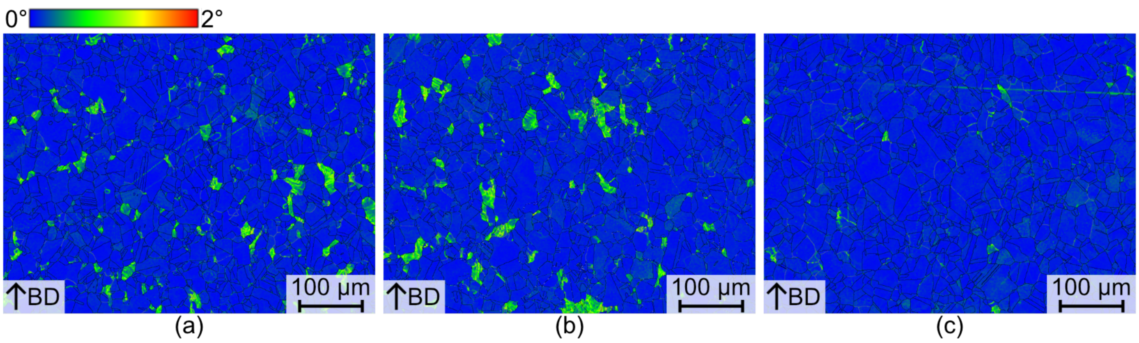

Figure 4.5: KAM maps that shows local distortion of the lattice within grains for samples from print B (a) SA 4 h, (b) SR+SA 4 h and (c) SA 24 h.

The KAM maps in Fig. 4.5 show predominately low local misorientation indicated by the blue. The two annealed for 4 h appears similar while the 24 h sample has less local misorientation, this is further confirmed by mean orientation spread in Table 4.4.

Table 4.4: Obtained from EBSD measurements for print B, the mean orientation spread represents the average crystallographic distortion within a grain relative to its mean orientation. <2° is considered recrystallized for a grain.

Condition	SA 4 h	SR+SA 4 h	SA 24 h
Mean orientation spread <2° [%]	93.7	94.3	96.7

4.3 Influence of part geometry on microstructure after heat treatment

To determine the impact of part geometry on recrystallization behavior after heat treatment, 10 mm cubes as well as thin walls (10×10 mm square) of varying thickness were printed.

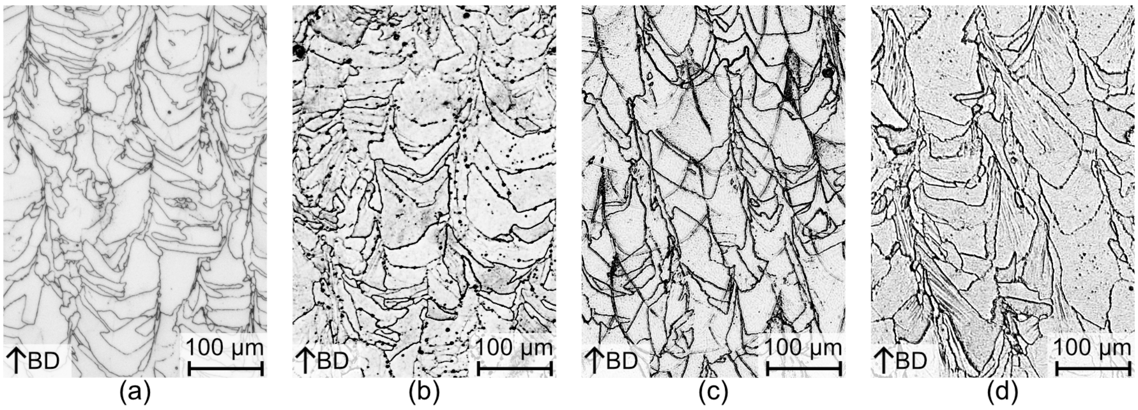

Figure 4.6: LOM images of etched samples produced from VIGA powder at 300 W laser power: (a) 10 mm cube in the SR (900 °C for 30 min) condition, (b) 10 mm cube in the SR+SA(1200 °C for 4 h) condition, (c) 2 mm thick thin wall in the SR condition and (d) 2 mm thick thin wall in the SR+SA condition.

Figure 4.6 shows the bulk microstructure of each sample in BD-plane, the cube in SR condition (Fig. 4.6a) exhibits columnar grains originating from the printing process and after annealing (Fig. 4.6b) the grain structure is largely retained. The 2 mm thick thin wall a similar evolution with most of the original grain structure observed in the SR condition (Fig. 4.6c) remains after following solution annealing (Fig. 4.6d). No apparent difference in recrystallization due to part geometry.

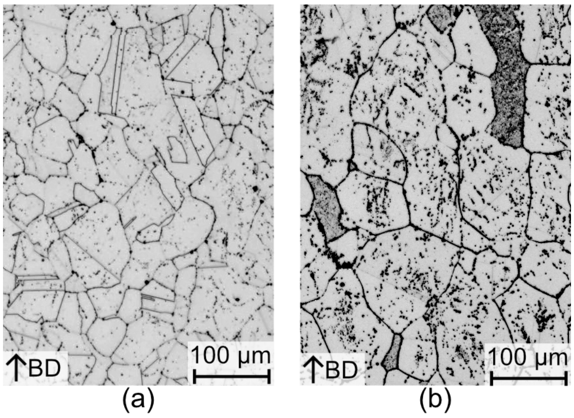

Figure 4.7: Optical microscope images of etched samples in the SA condition (1200 °C for 4 h) printed using GA powder: (a) 10 mm cube and (b) 0.5 mm thick thin wall.

Figure 4.7a shows the bulk region of the etched cube printed using GA powder and solution annealed at 1200 °C for 4 h. The microstructure exhibits a high degree of recrystallization characterized by the absence of parent grain (observed in Fig. 4.6a and b) as well as the presence of annealing twins. The 0.5 mm thick thin wall (Fig. 4.7b) exhibits a similar recrystallized grain structure where annealing twins appear as faint strait lines. The density of particulates seems higher in the thin wall than cube, although variations in etching should be considered. During water quenching, thin walls with thickness of 1 mm and below were susceptible to warping and the 0.5 mm thin wall was warped to a curvature of $\kappa = 0.0379\ \mathrm{mm}^{-1}$.

4.4 Grain size development during heat treatment

Grain size measurements were performed using the Frangi vesselness script and verified by EBSD on selected samples. Results are expressed as the equivalent diameter, i.e. the diameter of a circle with the same area as the measured grain.

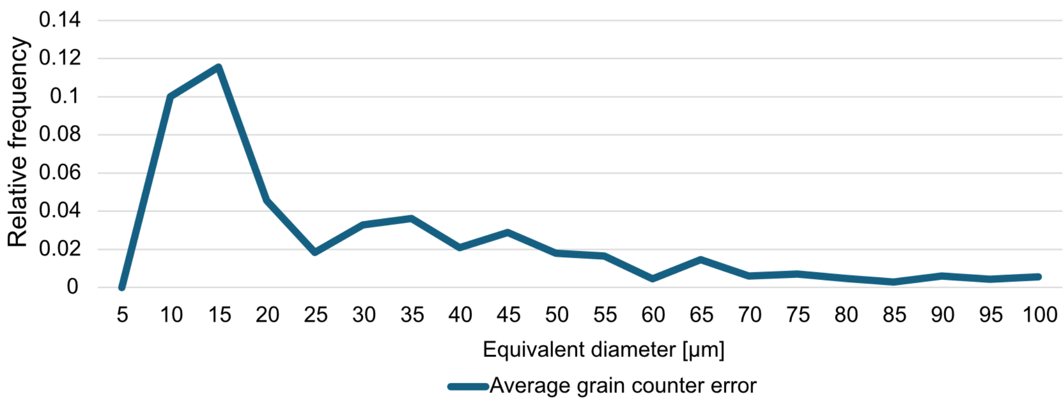

Figure 4.8: Average deviation of the grain counting script relative to EBSD-derived reference data.

Figure 4.8 shows the average deviation of the grain counter script based on Frangi vesselness filter from data obtained by EBSD and highlights discrepancy in the finer grain region.

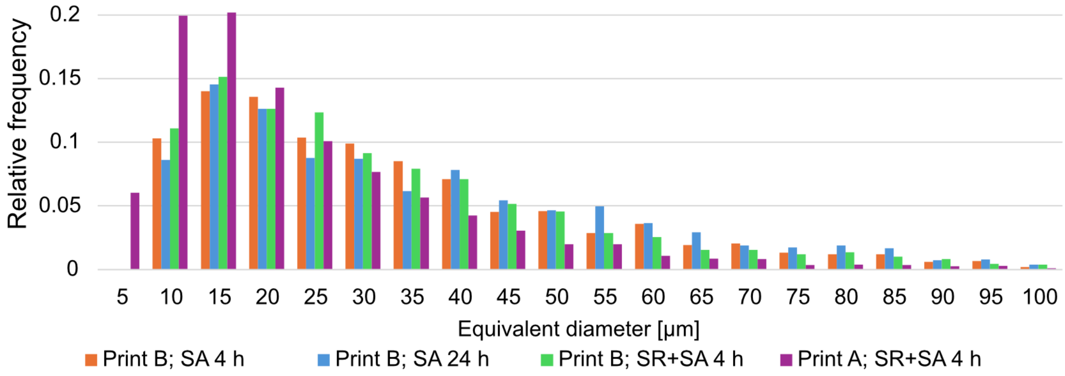

Figure 4.9: Histogram of equivalent diameter of grains in samples in both print A and B obtained by EBSD.

The grain size distributions in Fig. 4.9 show that samples from print B contain a larger proportion of coarse grains compared to the sample from print A, with median equivalent diameters given in Table 4.5. It should be noted that all samples in print B exhibited a high degree of recrystallization (Table 4.4), whereas the sample from print A did not (Table 4.2).

Table 4.5: Median equivalent diameter of selected samples, obtained by EBSD measurements.

Sample group	Print B			Print A
Condition	SA 4 h	SA 24 h	SR+SA 4 h	SR+SA 4 h
Median equivalent diameter [µm]	25.73	27.55	24.51	16.16

4.5 Chemical analysis of powders and printed parts

Table 4.6: Levels of oxygen and nitrogen in powder and printed part measured by combustion.

		Oxygen		Nitrogen	
	Measurements	Average [ppm]	Standard deviation [ppm]	Average [ppm]	Standard deviation [ppm]
316L NG 15-63 µm VIGA	3	219	2	473	5
Print A (VIGA)	2	260	4	482	3
316L 20-53 µm GA	3	685	23	1003	15
Print B (GA)	2	606	2	317	1

Table 4.6 shows the oxygen and nitrogen content of the powders used in this study and the printed parts produced from these powders. The VIGA powder analyzed was in its virgin state and the GA powder was recycled from two previous print cycles. The elemental contents of the powders were largely retained in the printed parts with the exception for nitrogen in print B.

5
Discussion

Several parameters influence the recrystallization behavior of PBF-LB produced 316L SS, and a few have been explored in this work; however, gaps in understanding remain.

Although the initial parameter study suggested that melt pool geometry may affect recrystallization behavior, the observed differences were not sufficient to justify further investigation within the scope of this work. Furthermore, the LoF porosity (Fig. 4.1d) presents challenges with respect to both mechanical performance and geometrical stability (see Section 2.1.3).

5.1 Effects of multiple variables on comparability between the print campaigns

Comparing results between the two print campaigns, one produced using VIGA powder in the as-received condition with both printing and heat treatment performed by an external manufacturer, and the other produced in-house using GA powder with subsequent heat treatment performed internally, should be approached with caution due to the large number of variables that may influence the outcome. In particular, the different atomization routes are expected to produce powders with distinct characteristics (Section 2.1.2) and different oxygen and nitrogen contents (Table 4.6). The two systems originate from different printer platforms, and the heat treatments were carried out under different atmospheres (vacuum versus argon). Consequently, it is difficult to isolate the effect of any single parameter. Therefore, any direct comparison of the response to heat treatment between the two builds should be interpreted with caution.

5.2 Degree of recrystallization

As stated in Section 2.2.1, the degree of recrystallization of PBF-LB produced parts after heat treatment is suggested to be strongly influenced by the GND density. This claim by Gao et al. would imply that the initial stress relief treatment applied to all the samples in print A could inhibit the recrystallization during subsequent solution annealing [11]. This is particularly relevant given that these samples showed no significant signs of recrystallization, despite the general consensus in the literature that 4 h solution anneal at 1200 °C is sufficient to produce a recrystallized microstructure.

Since print B exhibited a very similar response to print A samples after stress relieve, but after the subsequent SA, the absence of recrystallization cannot be attributed solely to the reduction in GND density caused by a SR cycle. However, Table 4.3 shows that in print B, there are fewer twin boundaries in the SR+SA 4 h condition than without SR. Suggesting a stress relieve cycle slightly inhibits the formation of Σ3 GBs, in line with Section 2.2.3 and explained by Jin et al., the formation of annealing twins is promoted by high stored strain [39].

Degree of recrystallization overall is high for all annealed samples in print B as evidenced by the EBSD data in Table 4.4, where the fraction of grains with mean orientation spread below 2° exceeds 93% across all solution annealed conditions. This stands in contrast to print A, where the SR+SA condition yielded only 60.9% of grains with mean orientation spread less than 2° (Table 4.2), this trend was also observed in LOM. The divergence is striking given that samples subjected to nominally identical HT protocols with SR and SA, this suggests that the dominant variable governing recrystallization is the feedstock when comparing print A with print B.

5.3 Powder chemistry as governing driving forces for recrystallization

The most prominent variable between print A and B is the powder atomization method. VIGA powder is melted under vacuum prior to atomization, while GA is melted in open air, resulting in measurable differences in chemical composition, as shown in Table 4.6. The GA powder contains higher levels of oxygen (685 ppm compared to 219 ppm for VIGA) and nitrogen (1003 ppm compared to 473 ppm for VIGA), these levels are roughly carried over to the printed parts with the exception for print B using GA powder where nitrogen levels were significantly lower. These interstitial elements are known to congregate and form inclusions during solidification [27], and the high particulate density observed in annealed samples in print B (Section 4.2.2) is consistent with this. Since these particulates are less frequent in the SR condition Fig. 4.3 (b, g) the elements are finer and more dispersed. These second phase particles can coarsen by Ostwald ripening and act as a nucleation point via particle stimulated nucleation (PSN) in the recrystallization process, so long they reach of sufficient size of 1 µm (Section 2.2.4) [46].

The low oxygen level and consequently low second phase particle density in print A could be the culprit by particles agglomerating but not reaching critical size to activate PSN. This would explain why samples from print B using GA powder recrystallize so extensively under conditions where the samples from print A using VIGA powder do not. However, this interpretation should be confirmed by printing and heat treating using VIGA powder under the exact conditions in print B or vice versa to eliminate any doubt arisen from variables mentioned in Section 5.1.

5.4 Effect of stress relieve on recrystallization and twin formation

The comparison of SR+SA and SA 4 h conditions in print B provides a controlled basis for assessing the role of the prior stress relieve. Across all EBSD metrics and under LOM, the differences are modest. Recrystallized fraction obtained by mean orientation spread (Table 4.4) is slightly higher in SR+SA condition (94.3%) than in the SA 4 h condition (93.7%), and the KAM maps (Fig. 4.5 a, b) show no qualitative distinction in residual lattice distortion between the two conditions. This suggests that, for GA powder at least, the stress relieve cycle does not prevent nor significantly inhibit recrystallization during the subsequent solution anneal. This is not in line with the theory of Gao et al. that GND density is the primary driver of recrystallization for PBF-LB parts [11].

A more telling difference is observed in the twin boundary fraction. Table 4.3 shows that the SR+SA condition produces fewer Σ3 boundaries (39.7%) than both SA 4 h (43.8%) and SA 24 h (44.3%). This is consistent with the theory proposed by Jin et al., that annealing twin formation is promoted by high stored strain during the early stages of recrystallization [39]. A stress relieve at 900 °C does not trigger recrystallization but does recover dislocation substructure, thereby reducing the driving force for annealing twin formation during the subsequent solution anneal. From a GBE perspective the difference between 40% and 44% could affect the connectivity of random HAGB (non CSL HAGB) network. A lower fraction of Σ3 boundaries is expected to increase random HAGB connectivity, which may in turn increase susceptibility to intergranular corrosion and stress corrosion cracking. This may therefore be relevant when assessing suitability for nuclear applications.

5.5 Grain boundary engineering

The results collectively highlight a fundamental challenge for GBE in PBF-LB austenitic stainless steel. The inability to process conventionally by deformation leads to the only stored energy available to drive recrystallization and twin nucleation entirely derives from the printing process. In GBE for conventional 316L, iterative deformation and annealing cycles are used to progressively increase the Σ3 boundary fraction and disrupt the random boundary network [12]. In PBF-LB this method is not possible while retaining the as-built near-net-shape.

The data from print B demonstrate that it is possible to achieve a high degree recrystallization and Σ3 boundary fractions greater than 40% through direct solution annealing. As seen in Table 4.3, the Σ3 fraction seems to reach a plateau before 4 h at 1200 °C rather than linear increase (43.8% after 4 h and 44.3% after 24 h), and the grain size increase is marginal (Table 4.5 and Fig. 4.9) between the two annealing durations. This saturation of twin boundary fraction and grain size suggests that extended annealing promotes recrystallization of grains with random grain boundaries rather than further nucleation of annealing twins or grain growth. The high density of particulates observed throughout samples in print B located both within grains and at GBs is likely a contributor to this effect by Smith-Zener pinning (Section 2.2.4), whereby second phase particles exert a retarding force on migrating grain boundaries that opposes the driving forces for grain growth. This is consistent with the theoretical condition for twin formation requiring migrating GBs and stored stresses [37] and would explain the plateau in $\Sigma3$ fraction. Conventional GBE of austenitic stainless steel utilizes iterative deformation and anneal cycles to circumvent this limitation by the reintroduction of stored strain energy that reactivates GB migration in each cycle [12]. In PBF-LB, deformation is not an option without compromising the geometry of the already near-net-shaped product, particle inclusions inherited from the powder feedstock and printing process might impose a practical upper limit on the achievable twin boundary fraction through thermal treatment alone. Notably, the $\Sigma3$ boundary fractions achieved in solution annealed GA samples (43-44% Table 4.3) exceed the typical twin boundary fraction of conventionally solution annealed 316L (>30% [38]), suggesting that direct solution annealing of PBF-LB 316L using GA powder can achieve a GB character distribution comparable to or exceeding that of its wrought counterpart without any deformation step.

5.6 Image analysis based on LOM vs EBSD data

Quantitative grain analysis based on LOM images processed with Frangi vesselness filter offers a time and cost-efficient alternative to EBSD, but the comparisons with EBSD derived data reveals limitations that must be considered when interpreting the results.

As shown in Fig. 4.8, the deviation between the two methods is most pronounced in the fine grain regime, with errors in the range of 10-12% for grains below approximately 20 µm in equivalent diameter, decreasing progressively for coarser grains. This size dependent discrepancy likely arises from several compounding factors. In the fine grain regime, closely spaced grain boundaries may not be fully resolved or merged during contrast enhancement, or grains can be merged due to discontinuous grain boundaries that the Frangi filter fails to recognize. Additionally, will different types of GBs etch differently, highly structured CSL boundaries like annealing twin boundaries will appear fainter than others. It should be noted that the EBSD data referenced does carry some of these problems related to grain merging and step size resolution restraints, meaning the apparent error in Fig. 4.8 reflects inaccuracies in both methods.

For coarser grains, the agreement between the two methods are considerably better, suggesting that the Frangi-based script is adequate for comparisons where trends in grain size is of primary interest rather than absolute values and samples etch similarly. However, the method is less reliable for microstructures with a large fraction of fine grains such as those in stress relived condition and should be used with caution in those cases. Further development, including optimization of the Frangi scale range, thresholding parameters and gap-closing logic, as well as standardization for etching, would be needed before the method can be considered a robust standalone tool for grain size quantification across the full range of microstructures encountered in PBF-LB 316L.

6 Conclusion

In this work, the influence of process parameters, powder feedstock, part geometry and heat treatment route on the microstructural development of PBF-LB 316L stainless steel was investigated. The study revealed clear differences in recrystallization behavior for samples produced by VIGA and GA following similar heat treatments. The following conclusions can be drawn:

- Powder feedstock had a dominant influence on recrystallization behavior. Samples produced using GA powder reached 93.7–96.7% recrystallized grains (MOS $< 2°$) after solution annealing, compared to only 60.9% for samples produced using VIGA powder under nominally identical conditions. The difference is proposed to stem from the higher oxygen content in GA powder generating a greater second phase particle density, which upon annealing coarsens through Ostwald ripening to reach the critical size for particle stimulated nucleation (PSN), a threshold not reached in VIGA samples.
- Recrystallization and twin formation in samples produced using GA powder were largely complete within the first 4 h of solution annealing at 1200 °C, with extended annealing to 24 h producing only marginal changes in grain size and Σ3 boundary fraction (43.8% to 44.3%). Suggesting a practical upper limit for Σ3 boundary formation through thermal treatment alone and high thermal stability of the grain structure.
- A prior stress relief cycle slightly reduced Σ3 boundary formation during subsequent solution annealing (43.8% SA vs. 39.7% SR+SA), attributed to partial dislocation recovery reducing the stored strain energy available to drive twin formation.
- Part geometry showed minimal influence on recrystallization.
- The Frangi-based image analysis method showed reasonable agreement with EBSD for larger grains but exhibited deviations of approximately 10–12% for grain sizes below 20 µm, indicating that further optimization is required before the method can be used as a standalone characterization tool.

Bibliography

[1] Anton du Plessis, Chris Broeckhoven, Ina Yadroitsava, Igor Yadroitsev, Clive H. Hands, Ravi Kunju, and Dhruv Bhate. Beautiful and Functional: A Review of Biomimetic Design in Additive Manufacturing. *Additive Manufacturing*, 27 (March):408–427, 2019. ISSN 22148604. doi: 10.1016/j.addma.2019.03.033. URL `https://doi.org/10.1016/j.addma.2019.03.033`.

[2] Igor Yadroitsev, Anton Du Plessis, and Ina Yadroitsava. Basics of laser powder bed fusion. *Fundamentals of Laser Powder Bed Fusion of Metals*, pages 15–38, jan 2021. doi: 10.1016/B978-0-12-824090-8.00024-X. URL `https://www.sciencedirect.com/science/chapter/edited-volume/pii/B978012824090800024X`.

[3] Levente Czégé, Daniel Nemes, David Huri, and Tamas Mankovits. Application of Additive Manufacturing Technology in Nuclear Power Plant Maintenance with Special Focus on Mechanical Properties. *Mecánica Computacional*, 42 (12):981–988, 2025. doi: 10.70567/mc.v42.ocsid8391.

[4] International Atomic Energy Agency. Adapting the energy sector to climate change / International Atomic Energy Agency. Technical report, International Atomic Energy Agency, Vienna, 2019.

[5] Mohsen Attaran. The rise of 3-D printing: The advantages of additive manufacturing over traditional manufacturing. *Business Horizons*, 60(5):677–688, sep 2017. ISSN 0007-6813. doi: 10.1016/J.BUSHOR.2017.05.011. URL `https://www.sciencedirect.com/science/article/pii/S0007681317300897`.

[6] Olivia Borgue, Jakob Müller, Alexander Leicht, Massimo Panarotto, and Ola Isaksson. Constraint replacement-based design for additive manufacturing of satellite components: Ensuring design manufacturability through tailored test artefacts. *Aerospace*, 6(11), 2019. ISSN 22264310. doi: 10.3390/aerospace6110124.

[7] Majid Laleh, Esmaeil Sadeghi, Reynier I. Revilla, Qi Chao, Nima Haghdadi, Anthony E. Hughes, Wei Xu, Iris De Graeve, Ma Qian, Ian Gibson, and Mike Y. Tan. Heat treatment for metal additive manufacturing. *Progress in Materials Science*, 133(July 2022):101051, 2023. ISSN 00796425. doi: 10.1016/j.pmatsci.2022.101051. URL `https://doi.org/10.1016/j.pmatsci.2022.101051`.

[8] F. C. Pinto, L. S. Aota, I. R. Souza Filho, D. Raabe, and H. R.Z. Sandim. Recrystallization in non-conventional microstructures of 316L stainless steel pro-

duced via laser powder-bed fusion: effect of particle coarsening kinetics. *Journal of Materials Science*, 57(21):9576–9598, 2022. ISSN 15734803. doi: 10.1007/s10853-021-06859-1. URL `https://doi.org/10.1007/s10853-021-06859-1`.

[9] Ming Luo, Hao Wang, Vitor V. Rielli, Xiaozhou Liao, Simon P. Ringer, Sophie Primig, and Nima Haghdadi. Grain boundary character evolution in stainless steel 316L upon laser powder-bed fusion and post-process heat treatment. *Materials Science and Engineering: A*, 927:148029, apr 2025. ISSN 0921-5093. doi: 10.1016/J.MSEA.2025.148029. URL `https://www.sciencedirect.com/science/article/pii/S0921509325002473`.

[10] Shubo Gao, Zhiheng Hu, Martial Duchamp, P. S.Sankara Rama Krishnan, Sravya Tekumalla, Xu Song, and Matteo Seita. Recrystallization-based grain boundary engineering of 316L stainless steel produced via selective laser melting. *Acta Materialia*, 200:366–377, 2020. ISSN 13596454. doi: 10.1016/j.actamat.2020.09.015. URL `https://doi.org/10.1016/j.actamat.2020.09.015`.

[11] Shubo Gao, Zhi Li, Steven Van Petegem, Junyu Ge, Sneha Goel, Joseph Vimal Vas, Vladimir Luzin, Zhiheng Hu, Hang Li Seet, Dario Ferreira Sanchez, Helena Van Swygenhoven, Huajian Gao, and Matteo Seita. Additive manufacturing of alloys with programmable microstructure and properties. *Nature Communications*, 14(1), 2023. ISSN 20411723. doi: 10.1038/s41467-023-42326-y.

[12] Valerie Randle and Gregory Owen. Mechanisms of grain boundary engineering. *Acta Materialia*, 54(7):1777–1783, apr 2006. ISSN 13596454. doi: 10.1016/j.actamat.2005.11.046. URL `https://doi.org/10.1002/pssa.2211310216`.

[13] Chang Ye, Chaoyi Zhang, Jingyi Zhao, and Yalin Dong. Effects of Post-processing on the Surface Finish, Porosity, Residual Stresses, and Fatigue Performance of Additive Manufactured Metals: A Review. *Journal of Materials Engineering and Performance*, 30(9):6407–6425, 2021. ISSN 15441024. doi: 10.1007/s11665-021-06021-7. URL `https://doi.org/10.1007/s11665-021-06021-7`.

[14] Min Yi, Wei Tang, Yiqi Zhu, Chenguang Liang, Ziming Tang, Yan Yin, Weiwei He, Shen Sun, and Shaopu Su. A holistic review on fatigue properties of additively manufactured metals. *Journal of Materials Processing Technology*, 329:118425, aug 2024. ISSN 09240136. doi: 10.1016/j.jmatprotec.2024.118425.

[15] A. Leicht, M. Rashidi, U. Klement, and E. Hryha. Effect of process parameters on the microstructure, tensile strength and productivity of 316L parts produced by laser powder bed fusion. *Materials Characterization*, 159(6):110016, jan 2020. ISSN 10445803. doi: 10.1016/j.matchar.2019.110016. URL `https://doi.org/10.1007/s11665-014-0958-z`.

[16] Alexander Leicht, Uta Klement, and Eduard Hryha. Effect of build geometry on the microstructural development of 316L parts produced by additive manufacturing. *Materials Characterization*, 143:137–143, sep 2018. ISSN 10445803. doi:

10.1016/j.matchar.2018.04.040. URL https://doi.org/10.1016/j.matchar.2018.04.040.

[17] Ting Zhu and Wen Chen. Mechanical behaviour of additively manufactured metals. *Nature Materials*, 2026. ISSN 1476-1122. doi: 10.1038/s41563-025-02459-5. URL http://dx.doi.org/10.1038/s41563-025-02459-5.

[18] Sujit B. Chaudhari, Vishnu D. Wakchaure, Prashant N. Nagare, and Suraj B. Kadhane. Effect of solution annealing on the microstructure, mechanical properties & residual stresses of selective laser melted Inconel 718. *Journal of Alloys and Compounds*, 1045(August):184656, 2025. ISSN 09258388. doi: 10.1016/j.jallcom.2025.184656. URL https://doi.org/10.1016/j.jallcom.2025.184656.

[19] Wenqi Li, Lixin Meng, Xiaofeng Niu, and Wei Zhou. Microstructure, mechanical properties, and deformation behaviour of LPBF 316L via post-heat treatment. *Virtual and Physical Prototyping*, 19(1):1–19, 2024. ISSN 17452767. doi: 10.1080/17452759.2024.2405623. URL https://doi.org/10.1080/17452759.2024.2405623.

[20] Yahya Aghayar, Ayda Shahriari, Mojtaba Shakerian, Mackenzie Purdy, and Mohsen Mohammadi. Microstructure tailoring of laser powder bed fused 316L impellers for enhanced mechanical properties and optimum electrochemical characteristics through hot isostatic pressing. *Materials Science and Engineering: A*, 925:147916, mar 2025. ISSN 0921-5093. doi: 10.1016/J.MSEA.2025.147916. URL https://www.sciencedirect.com/science/article/pii/S0921509325001340.

[21] Enrique J. Lavernia, Kaka Ma, Julie M Schoenung, James F. Shackelford, and Baolong Zheng. *Metallic Powders for Additive Manufacturing: Science and Applications*. John Wiley & Sons, 2024. ISBN 9781119908135.

[22] Xiaona Ren, Yao Wang, Zhenfan Wang, Peng Wang, Zihao Wang, Lebiao Yang, Weifeng Qi, Xinggang Li, and Changchun Ge. Properties of Electrode Induction Melting Gas Atomization- and Vacuum Induction Melting Atomization-Produced Powders and Their As-HIPed Blanks. *Materials*, 18(3):1–13, 2025. ISSN 19961944. doi: 10.3390/ma18030710.

[23] Eduard Hryha. Powder for Metal Additive Manufacturing: Production, Reuse and Recycling. *Funtai Oyobi Fummatsu Yakin/Journal of the Japan Society of Powder and Powder Metallurgy*, 72:S83–S90, 2025. ISSN 05328799. doi: 10.2497/jjspm.14B-T6-03.

[24] D. Lindell. Texture evolution of warm-rolled and annealed 304L and 316L austenitic stainless steels. *IOP Conference Series: Materials Science and Engineering*, 82(1):8–12, 2015. ISSN 1757899X. doi: 10.1088/1757-899X/82/1/012101.

[25] Thomas Voisin, Jean Baptiste Forien, Aurelien Perron, Sylvie Aubry, Nicolas Bertin, Amit Samanta, Alexander Baker, and Y. Morris Wang. New insights

on cellular structures strengthening mechanisms and thermal stability of an austenitic stainless steel fabricated by laser powder-bed-fusion. *Acta Materialia*, 203:116476, jan 2021. ISSN 1359-6454. doi: 10.1016/J.ACTAMAT.2020.11.018. URL https://www.sciencedirect.com/science/article/pii/S1359645420308934.

[26] Luqing Cui, Shuang Jiang, Jinghao Xu, Ru Lin Peng, Reza Taherzadeh Mousavian, and Johan Moverare. Revealing relationships between microstructure and hardening nature of additively manufactured 316L stainless steel. *Materials and Design*, 198:109385, 2021. ISSN 18734197. doi: 10.1016/j.matdes.2020.109385. URL https://doi.org/10.1016/j.matdes.2020.109385.

[27] Xinliang Yang, Feng Gao, Fengzai Tang, Xinjiang Hao, and Zushu Li. Effect of Surface Oxides on the Melting and Solidification of 316L Stainless Steel Powder for Additive Manufacturing. *Metallurgical and Materials Transactions A: Physical Metallurgy and Materials Science*, 52(10):4518–4532, 2021. ISSN 10735623. doi: 10.1007/s11661-021-06405-3. URL https://doi.org/10.1007/s11661-021-06405-3.

[28] Zhong Hui. *The ECPH Encyclopedia of Mining and Metallurgy*. China Publishing House, 2024. doi: https://doi.org/10.1007/978-981-99-2086-0.

[29] Qian Xiao, Junjie Chen, Hyeon Bae Lee, Changheui Jang, and Kyungnam Jang. Effect of heat treatment on corrosion behaviour of additively manufactured 316L stainless steel in high-temperature water. *Corrosion Science*, 210:110830, jan 2023. ISSN 0010-938X. doi: 10.1016/J.CORSCI.2022.110830. URL https://www.sciencedirect.com/science/article/pii/S0010938X2200748X.

[30] Chenglu Tang, Jingfan Yang, Fan Zhang, Joseph W. Aroh, E. Steven Porterfield, Barton C. Prorok, and Xiaoyuan Lou. Twin-related grain boundary engineering of additively manufactured 316L stainless steel. *Acta Materialia*, 301 (1):121503, dec 2025. ISSN 13596454. doi: 10.1016/j.actamat.2025.121503. URL https://doi.org/10.1038/nmat5021.

[31] Luqing Cui, Cheng Han Yu, Shuang Jiang, Xiaoyu Sun, Ru Lin Peng, Jan Erik Lundgren, and Johan Moverare. A new approach for determining GND and SSD densities based on indentation size effect: An application to additive-manufactured Hastelloy X. *Journal of Materials Science & Technology*, 96:295–307, jan 2022. ISSN 1005-0302. doi: 10.1016/J.JMST.2021.05.005. URL https://www.sciencedirect.com/science/article/pii/S1005030221004965?via{%}3Dihub.

[32] Thale R. Smith, Joshua D. Sugar, Chris San Marchi, and Julie M. Schoenung. Strengthening mechanisms in directed energy deposited austenitic stainless steel. *Acta Materialia*, 164:728–740, feb 2019. ISSN 1359-6454. doi: 10.1016/J.ACTAMAT.2018.11.021. URL https://www.sciencedirect.com/science/article/pii/S1359645418308978?via{%}3Dihub.

[33] D. Riabov, A. Leicht, J. Ahlström, and E. Hryha. Investigation of the strengthening mechanism in 316L stainless steel produced with laser powder bed fusion.

Materials Science and Engineering: A, 822(June), 2021. ISSN 09215093. doi: 10.1016/j.msea.2021.141699.

[34] Niels Hansen. Hall–Petch relation and boundary strengthening. *Scripta Materialia*, 51(8):801–806, oct 2004. ISSN 13596462. doi: 10.1016/j.scriptamat.2004.06.002. URL https://doi.org/10.1080/14786436208201857.

[35] D. Riabov. *Laser-based powder bed fusion of stainless steels: Powder properties, processability and microstructure.* PhD thesis, Chalmers University of Technology, 2022.

[36] Siqi Chen, Guoqiang Ma, Guilin Wu, Andrew Godfrey, Tianlin Huang, and Xiaoxu Huang. Strengthening mechanisms in selective laser melted 316L stainless steel. *Materials Science and Engineering: A*, 832:142434, jan 2022. ISSN 09215093. doi: 10.1016/j.msea.2021.142434. URL https://www.sciencedirect.com/science/article/abs/pii/S092150932101697X.

[37] Nathalie Bozzolo and Marc Bernacki. Viewpoint on the Formation and Evolution of Annealing Twins During Thermomechanical Processing of FCC Metals and Alloys. *Metallurgical and Materials Transactions A*, 51(6):2665–2684, 2020. ISSN 1543-1940. doi: 10.1007/s11661-020-05772-7. URL https://doi.org/10.1007/s11661-020-05772-7.

[38] Weijiu Huang, Shanshan Yuan, Linjiang Chai, Luyao Jiang, Haiding Liu, Fangjun Wang, and Dongzhe Wang. Development of Grain Boundary Character Distribution in Medium - Strained 316L Stainless Steel During Annealing. *Metals and Materials International*, 25(2):364–371, 2019. ISSN 2005-4149. doi: 10.1007/s12540-018-0203-7. URL https://doi.org/10.1007/s12540-018-0203-7.

[39] Y. Jin, M. Bernacki, G. S. Rohrer, A. D. Rollett, B. Lin, and N. Bozzolo. Formation of annealing twins during recrystallization and grain growth in 304L austenitic stainless steel. *Materials Science Forum*, 753:113–116, 2013. ISSN 16629752. doi: 10.4028/www.scientific.net/MSF.753.113.

[40] Rajneesh Yadav and Nitin Kumar Sharma. Effect of twin-related coincident site lattice (CSL) boundaries and their network on strengthening and plasticity in 316L stainless steel. *Materials Science and Engineering: A*, 956:149893, mar 2026. ISSN 0921-5093. doi: 10.1016/J.MSEA.2026.149893. URL https://www.sciencedirect.com/science/article/abs/pii/S0921509326001735.

[41] Ke Huang, Knut Marthinsen, Qinglong Zhao, and Roland E. Logé. The double-edge effect of second-phase particles on the recrystallization behaviour and associated mechanical properties of metallic materials. *Progress in Materials Science*, 92:284–359, mar 2018. ISSN 0079-6425. doi: 10.1016/J.PMATSCI.2017.10.004. URL https://www.sciencedirect.com/science/article/abs/pii/S0079642517301287.

[42] Cyril Stanley Smith. No Grains, Phases, and Interfaces: An Interpretation of Microstructure. *Transactions of the Metallurgical Society of AIME*, 175:15–51, 1948.

[43] Clarence Zener. Theory of Growth of Spherical Precipitates from Solid Solution. *Journal of Applied Physics*, 20(10):950–953, 1949.

[44] Sebastian Florez and Marc Bernacki. Efficient and accurate simulation of the Smith–Zener pinning mechanism during grain growth using a front-tracking numerical framework. *Computational Materials Science*, 256:113958, jun 2025. ISSN 0927-0256. doi: 10.1016/J.COMMATSCI.2025.113958. URL https://www.sciencedirect.com/science/article/pii/S0927025625003015.

[45] Charlie Bevan, Thomas Jones, Amar Malla, James Sullivan, David Penney, and Robert Lancaster. The effects of recrystallisation on the fatigue and corrosion properties of LB-PBF stainless steel 316L. *Materials & Design*, 264:115768, apr 2026. ISSN 0264-1275. doi: 10.1016/J.MATDES.2026.115768. URL https://www.sciencedirect.com/science/article/pii/S0264127526003412.

[46] F. J. Humphreys. The nucleation of recrystallization at second phase particles in deformed aluminium. *Acta Metallurgica*, 25(11):1323–1344, nov 1977. ISSN 0001-6160. doi: 10.1016/0001-6160(77)90109-2. URL https://www.sciencedirect.com/science/article/abs/pii/0001616077901092.

[47] British Stainless Steel Association (BSSA). Stress relieving heat treatments for austenitic stainless steels. URL https://bssa.org.uk/bssa{_}articles/stress-relieving-heat-treatments-for-austenitic-stainless-steels/.

[48] SAE International. AEROSPACE MATERIAL SPECIFICATION, AMS 2759/4B, 2001.

[49] A Leicht. *Laser powder bed fusion of 316L stainless steel: Microstructure and mechanical properties as a function of process parameters, design and productivity.* PhD thesis, Chalmers University of Technology, 2020.

[50] Höganäs AB. PowderFinder. URL https://www.hoganas.com/en/powder-technologies/additive-manufacturing-metal-powders/powderfinder/.

Acknowledgements

This work would not have been possible without the support of several people to whom the author is sincerely grateful.

Supervisor Rasmus Gunnerek and Examiner Uta Klement at the Department of Industrial and Materials Science, Chalmers University of Technology, are greatly acknowledged for their supervision, guidance and valuable feedback throughout this work.

The author would also like to extend sincere thanks to Tommy Sand and Fredrik Gustavsson at Vattenfall for their generous contribution of time and expertise and for many valuable discussions throughout the project.

Petter Jacobsson, Gothenburg, June 2026

DEPARTMENT OF INDUSTRIAL AND MATERIALS SCIENCE
CHALMERS UNIVERSITY OF TECHNOLOGY
Gothenburg, Sweden
www.chalmers.se

CHALMERS
UNIVERSITY OF TECHNOLOGY